RSC Advances

Photoelectrochemical properties of PbS quantum dots sensitized TiO$_2$ nanorods

photoelectrodes

Limin Yu[a,b], Junhong Jia[1a*], Gewen Yi[2a*], Minmin Han[a,b]

[a]*State Key Laboratory of Solid Lubrication, Lanzhou Institute of Chemical Physics, Chinese Academy*

of Sciences, Lanzhou 730000, PR China

[b]*University of Chinese Academy of Sciences, Beijing 100039, PR China*

* Corresponding authors:

[1]Tel.: +86-931-4968611; fax: +86-931-4968163. Email: jhjia@licp.cas.cn

[2]Tel.: +86-931-4968135; fax: +86-931-4968135. Email: gwyi@licp.cas.cn

ABSTRACT

The semiconductor PbS quantum dots (QDs) were synthesized on TiO_2 nanorods (NRs) via successive ionic layer adsorption and reaction (SILAR) method. The deposition of PbS QDs on the TiO_2 NRs could enhance the ability of light absorption and improve the power conversion efficiency of solar cell. The morphological feature, crystal structures, optical properties, photoelectrochemical performances, electron transfer at the TiO_2-QDs/electrolyte interface and electron lifetime of the obtained PbS QDs/TiO_2 NRs photoelectrodes were characterized and discussed in detail. The results demonstrate that the photoelectrochemical performance of PbS QDs/TiO_2 NRs depends on the value of SILAR cycle number. The highest photoelectric conversion efficiency of 0.77% is achieved at the SILAR cycle number n = 4 under one sun illumination (AM 1.5, 100 mW cm^{-2}). The enlarge absorption edges to the visible region and the effective separation of photogenerated electron-hole pairs at the PbS QDs-TiO_2 NRs interface are attributed to the promotion of power conversion efficiency.

Keywords: successive ionic layer adsorption and reaction method; PbS quantum dot; semiconductor materials; quantum dot solar cells

1. Introduction

In recent decades, quantum dot sensitized solar cells (QDSSCs) as the third generation solar cells have attracted significant attention[1-4]. Although the power conversion efficiencies of QDSSCs lag behind those of dye-sensitized solar cells (DSSCs)[5], the particular nature properties of quantum dots (QDs) have added impetus to their promising application. On the basis of the quantum size effect, optical band gap of QDs can be tuned by accommodating QDs size, which enhances their ability to exploit the NIR region of the sunlight spectrum[2, 6]. On the other hand, the impact ionization effect makes the quantum yield to be more than 100% by generating multi-excitons from single optical

photon absorption[7], which enable their theoretical maximum thermodynamic conversion efficiency can

reach 44% instead of the 31% of the Schockley-Queisser detailed balance limit. These special

properties make QDSSCs as promising novel highly-efficient photovoltaic (PV) devices.

At present, TiO_2 is one of the most commonly used photoanode material for solar cells[8, 9]. Among

the TiO_2 nanostructured materials, well-aligned TiO_2 one-dimensional (1D) nanostructures, such as

nanorod[10, 11], nanotube[12] and nanowire[13], exhibit high photoelectrochemical performance in solar cells,

photocatalytic in water splitting[14-16] and degradation of organic pollutants due to their highly

well-defined 1D channel structure, relatively high surface area and unique charge transfer and

transportation properties. However, TiO_2 has a large band gap of 3.26 eV, which limits its visible light

utilization. Thereby, much effort has been devoted to construct novel hetero-composite structures to

enlarge the absorption of solar spectrum. One effective strategy is to combine TiO_2 with chalcogenide

semiconductor quantum dots, such as CdS[17], $CdSe$[18], Ag_2S[19], PbS[20], Bi_2S_3[21], $CuInS_2$[22] and so on. As an

important p-type chalcogenide compound, PbS QDs with high absorption coefficient, good

photostablity and bulk band gap of 0.41 eV, have been widely investigated for photoenergy conversion

applications. PbS QDs have been prepared using several methods, including chemical bath deposition

(CBD)[23], thermal evaporation[24], thermolysis[25] and successive ionic layer adsorption and reaction

$(SILAR)$[26]. In both principle and practice, the SILAR method can be considered as the best way to

deposit well-defined composition-modulated QDs layers onto metal oxides in the solution process with

the advantage of being a faster, more reproducible, and less expensive way to deposit sensitizing

materials[27, 28].

Herein, we report a facile method to deposit PbS QDs onto one-aligned TiO_2 nanorods for the first

time and investigate their photoelectric performance in assembled QDSSCs. The synthetic process does

not use particular instrument and does not need any pre-synthesis of the precursors. The influence of SILAR cycle numbers for the photoelectrochemical performance of the assembled QDSSCs has been investigated in details. The photocurrent density of the composite photoelectrode enhanced by 3-5 times than that of the bare TiO_2 NRs. The composite electrode results in an energy conversation efficiency of 0.77% with a short circuit current density of 5.39 mA cm^{-2} under illumination at 100 mW cm^{-2}.

2. Experimental section

2.1 Materials

Fluorine-doped tin oxide (FTO) glass (14 ohm per square), analytical-grade concentrated hydrochloric acid (HCl, 36.5%-38% by weight), lead nitrate ($Pb(NO_3)_2$, 99%), sodium sulfide ($Na_2S \cdot 9H_2O$, 99%), sulfur powder (S, 99.9%), sodium sulfite (Na_2SO_3, 99.5%), potassium chloride (KCl, 99.9%) and chloroplatinic acid ($H_2PtCl_6 \cdot 6H_2O$, 99%) were purchased commercially. Titanium chloride ($TiCl_4$, 99.5%) was purchased from Alfa. All chemicals were used without further purification.

2.2 Fabrication of PbS/TiO$_2$ NRs photoelectrodes

TiO_2 nanorod arrays were prepared on fluorine-doped tin oxide (FTO) glass using a hydrothermal method that was described in detail elsewhere[29, 30]. Typically, TiO_2 NRs film was dipped into 0.02 M $Pb(NO_3)_2$ aqueous solution for 60 s followed by deionzed water washing, and dipped into 0.05 M Na_2S aqueous solution for 60 s followed by deionzed water washing. The two-step dipping and rinsing procedure was termed as one SILAR cycle of PbS. The amount of PbS QDs can be increased by repeating the deposition cycle. In order to obtain optimized samples, different deposition cycles such as 3, 4, 5 and 6 times were applied to vary the amount of the PbS QDs assembled on the TiO_2 NRs. Finally, the obtained PbS QDs-TiO_2 NRs films were dried in nitrogen stream. The TiO_2 NRs

after n cycles of PbS QDs deposition was denoted as PbS(n)/TiO$_2$ NRs.

2.3 Cell fabrication

The Pt counter-electrode was prepared by spin-coating 5 mM H$_2$PtCl$_6$ 2-isopropyl solution onto a

FTO glass substrate with a hole per-drilled, followed by heating at 400 ℃ for 20 min. The

liquid-junction QDSSCs were fabricated by sandwiching the as-prepared PbS(n)/TiO$_2$ NRs

photoanodes and Pt counterelectrodes by placing a 60 μm-thick hot-melt polymer (Surlyn, DuPont)

material as a spacer. The inter-electrode space was filled with redox electrolyte consisting of 1.0 M

Na$_2$S, 2.0 M sulfur and 0.2 M KCl in the mixture of methanol and water solution (7:3 by volume) by

vacuum back-filling through a hole per-drilled in the counter electrode, and then the hole was sealed

employing the hot-melt polymer and slide glass. The active area of QDSSCs was 0.5 cm^2.

2.4 Measurements

Field emission scanning electron microscope (FESEM, JSM-6701F, Japan), transmission

electron microscope and high-resolution transmission electron microscope (TEM, JEOLJEM-1210)

were employed for a close insight into the morphology of the PbS/TiO$_2$NRs. The structure and

phase composition of the samples were studied by X-ray diffractometry (XRD) recorded using an

X-ray diffractometer (Rigaku D/max-2400, Japan) with Cu-K$_\alpha$ radiation (λ = 0.15418 nm) at a

speed of 5° min^{-1}. UV–visible absorbance spectra of the samples were obtained using a UV–visible

spectrophotometer (Shimadzu UV-2600 spectrophotometer). The chemical states of the elements

were determined using X-ray photoelectron spectroscope (XPS, ESCALAB 250Xi, Thermo Scientific),

and the binding energy of contaminated carbon (C 1s = 284.8 eV) was used as reference. A computer

controlled electrochemical workstation (CH Instruments, CHI 660d) was used for the

photoelectrochemical (PEC) measurements, which were measured in an electrochemical cell under

one sun illumination (AM 1.5, 100 mW cm^{-2}) in 0.05 M Na$_2$S and 0.95 M Na$_2$SO$_3$ electrolyte solution with a three-electrode system, in which PbS/TiO$_2$ NRs electrodes, a platinum wire and saturation mercury electrode (SCE) were used as the working electrode, the counter electrode and reference electrode, respectively. Photocurrent-voltage measurements were performed with a computer-programmed Keithley 2610 Souremeter at room temperature under illumination of simulated sunlight (CELL-S500, China, AM1.5, 100 mWcm^{-2}). The incident light was calibrated with a reference silicon solar cell (CEL-RCCO, China). All photoelectrochemical experiments were carried out under ambient conditions.

3 Results and discussion
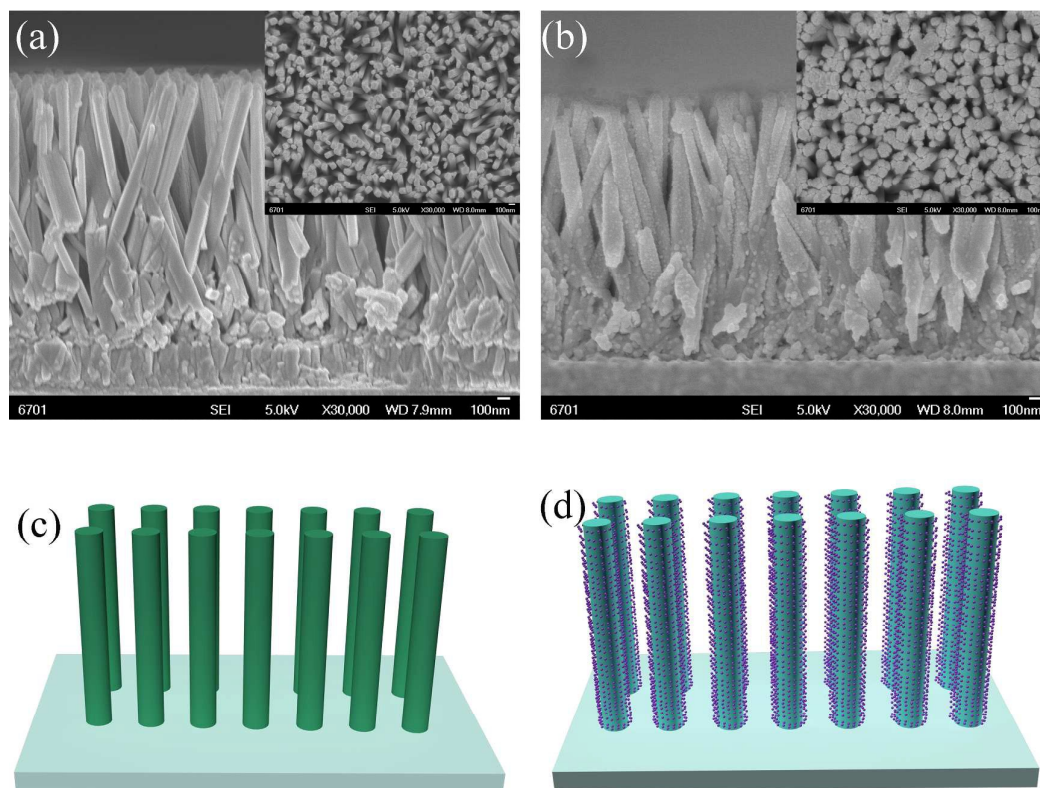
Fig. 1 Cross-sectional view FESEM images of (a) TiO$_2$ NRs, (b) PbS(4)/TiO$_2$ NRs (The insets show the top-view of the corresponding Cross-sectional view FESEM images). 3D schematic diagrams of (c) TiO$_2$ NRs, (d) PbS(4)/TiO$_2$ NRs.

Fig. 1 shows the FESEM images of the TiO_2 NRs and PbS(4)/TiO_2 NRs (a-b) and the

corresponding 3D schematic diagrams (c-d). Almost all TiO_2 NRs are vertically aligned with relatively

smooth sides and have a uniform length of 2 μm (Fig. 1a). The top-view shows that although the

density of TiO_2 NRs is high, there is still obviously porosity between them(inset of Fig. 1a). The

surface of TiO_2 NRs becomes rough after PbS QDs uniformly coated on the TiO_2 NRs and the

deposition of PbS QDs does not destroy the morphology of TiO_2 NRs (Fig. 1b).
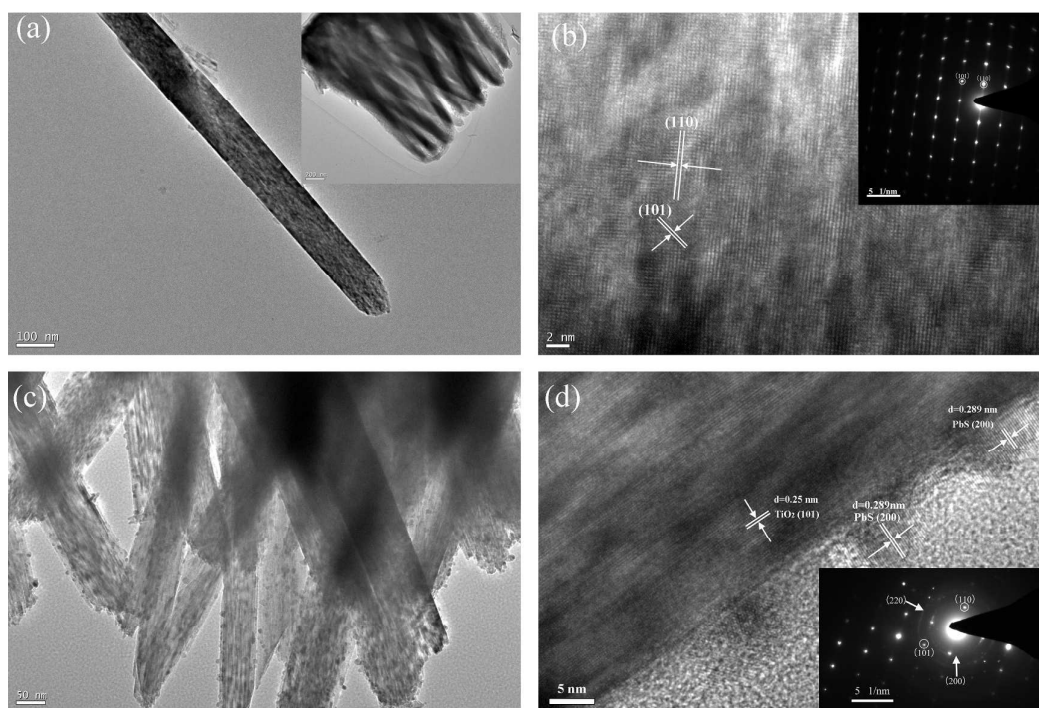
Fig.2 TEM images of plain TiO_2 NRs (a) and PbS(4)/TiO_2 NRs (c). The inset in (a) is a bunch of TiO_2 NRs.

HRTEM images of the corresponding TiO_2 NRs (b) and PbS(4)/TiO_2 NRs (d). The insets in (b) and (d) are the

corresponding selected-area electron diffraction pattern, respectively.

The TEM and HRTEM images of TiO_2 NRs and PbS(4)/TiO_2 NRs are demonstrated in Fig. 2. The

average diameter and length of TiO_2 NRs are 100 ± 5 nm and 2.1 ± 0.1 μm, respectively. It is

completely crystalline along entire length (Fig. 2b), and the electron diffraction micrograph (inset)

confirming their single-crystalline nature. The observed distinguishable interplanar spacing of 0.25 nm

and 0.35 nm are corresponded to the lattice fringe values for the (101) and (110) lattice planes of

tetragonal rutile TiO_2, respectively. The PbS QDs with a size ranging from 5 nm to 8 nm are uniformly

adsorbed on the TiO_2 NRs (Fig. 2c). The observed 0.289 nm lattice fringe in high-resolution TEM and

selected area electron diffraction (Fig. 2d) can be assigned to the (220) planes of the cubic PbS.
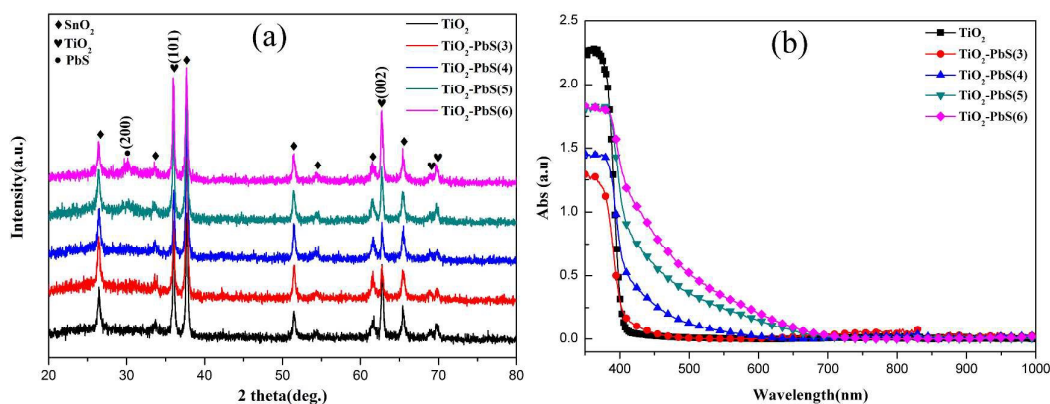
Fig. 3 Typical XRD patterns (a) and UV-Vis absorption spectra (b) of the bare TiO_2 NRs and as-prepared

$PbS(n)/TiO_2$ photoelectrodes.

Fig. 3a shows typical XRD spectrums of the bare TiO_2 NRs and as-prepared $PbS(n)/TiO_2$

photoelectrodes. Apart from the FTO substrate, the rest of the diffraction peaks match well with the

tetragonal rutile TiO_2 (JCPDS file No.71-0650) and cubic PbS (JCPDS file No. 78-1057), respectively.

The main diffraction peaks located at 36.1° and 62.7° are assigned to the crystal planes of (101) and

(002) of TiO_2 NRs. Meanwhile, the main diffraction peaks located at 30.1° can be ascribe to the crystal

planes of (200) of PbS QDs. It can also be seen that the main peak of PbS phase enhances gradually

along with the increase of SILAR cycle. The XRD peaks of cubic PbS phase are broad, suggesting that

the size of the deposited PbS crystallites on the surface of TiO_2 NRs is very small. The average

diameter of PbS QDs estimated by Scherrer's equation is about 8 nm, which is accordance with the

HRTEM result shown in Fig. 2d. Fig. 3b shows the UV-Vis absorption spectra of PbS/TiO_2 NRs fabricated with different SILAR cycles. The TiO_2 NRs only absorb the high energy light with a wavelength shorter than 400 nm, while the deposition of PbS QDs on TiO_2 NRs enlarged the absorption edges from 400 nm to 700 nm due to the narrow bandgap of PbS. The increasing in absorption for the visible light after each SILAR cycle are corresponding to that the amount increasing of deposition PbS nanoparticles. However, given that most Ⅱ-Ⅵ semiconductor materials have large hole masses, strong quantum confinement can be difficult to achieve[25]. And the devoid of significant absorption peak indicates the absorption is negligible band-edge absorption.
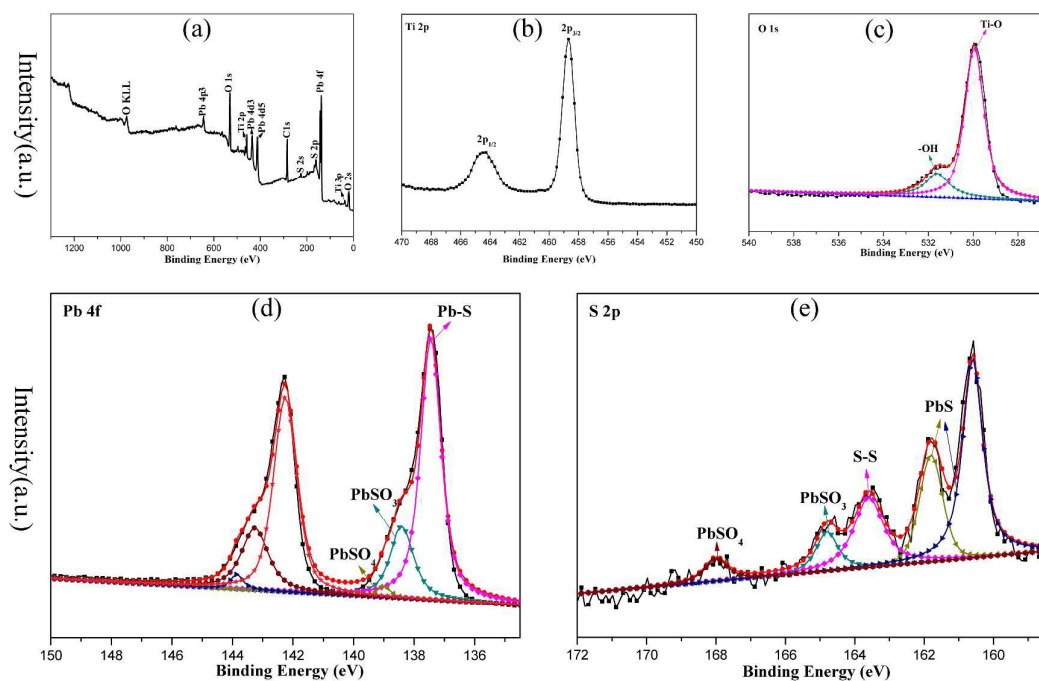
Fig. 4 XPS spectra of $PbS(4)/TiO_2$: (a) survey spectrum, (b) Ti 2p, (c) O 1s, (d) Pb 4f, (e) S 2p. The deconvolution of O 1s, Pb 4f and S 2p spectras were performed by fitting a sum of Gaussian-Lorentzian functions to the experimental data on Multipak software. The black curves are the experimental data and the red curves are the sum of curve fitting.

Table 1 Binding energy, chemical species and atomic percentages of as-prepared $PbS(4)/TiO_2$.

Elements	Binding Energy (eV)	Species	Atomic(%)
	137.4	PbS	74.3
Pb	138.4	$PbSO_3$	23.6
	139.0	$PbSO_4$	2.1
	160.6	PbS	42.6
	161.8	PbS	21.5
S	163.6	S-S	21.8
	164.8	$PbSO_3$	8.7
	168.0	$PbSO_4$	5.3

The surface composition as well as valence state of as-prepared PbS(4)/TiO_2 were determined by

XPS (Fig. 4 a-e). The survey spectrum confirms the existence of Pb, S, Ti and O elements in the sample

(Fig. 4a). The peaks of the binding energies at 464.40 eV and 458.71 eV are assigned to the $2p_{1/2}$ and

$2p_{3/2}$ of Ti^{4+} (Fig.4d). The characteristic peaks at 531.6 eV and 529.9 eV can be seen in the

high-resolution O1s spectra (Fig. 4c). The former peak is closely related to the hydroxyl groups (-OH)

resulting mainly from the chemisorbed water[31], and the later peak is described to the O atom bound to

Ti^{31}. As we all known, the surface energy of quantum dots is high, which make them can be oxidized

easily in the ambient conditions. To evaluate the Pb-S species, we focused on the Pb 4f and S 2p XPS

to analyze oxidation species (Fig. 4d-e). Detailed spectral deconvolution of the high resolution XPS

spectra allowed us to distinguish the sulfur-containing oxidation species such as lead sulfite ($PbSO_3$),

lead sulfate ($PbSO_4$) and polythiol (S-S)[32]. The abundance ratio of the sulfur-containing oxidation

products were presented in table 1. The QDs consisted of 74.3% PbS, 23.6% $PbSO_3$ and 2.1% $PbSO_4$

from Pb 4f spectra, whereas 64.1% PbS, 8.7% $PbSO_3$ and 5.3% $PbSO_4$ from S 2p spectra. The ratio

distinction between two spectra is mainly from polythiol product, which does not contain Pb element.

But there is no accurate data to prove the effection of polythiol product for reducing the value of band

gap. To our best knowledge, $PbSO_3$ and $PbSO_4$ can introduce trap states lying 0.1 and 0.3 eV below the

conduction band, respectively[33, 34]. The trap states with depth of 0.1 eV introduced by $PbSO_3$ are

relatively shallow and operate mainly to extend the effective carrier lifetime, which are compatible

with the device performance. However, the trap states with depth of 0.3 eV introduced by $PbSO_4$ are

relatively deep and operate mainly as catastrophic recombination centers, which lead to midgap

recombination and consequent loss of performance.
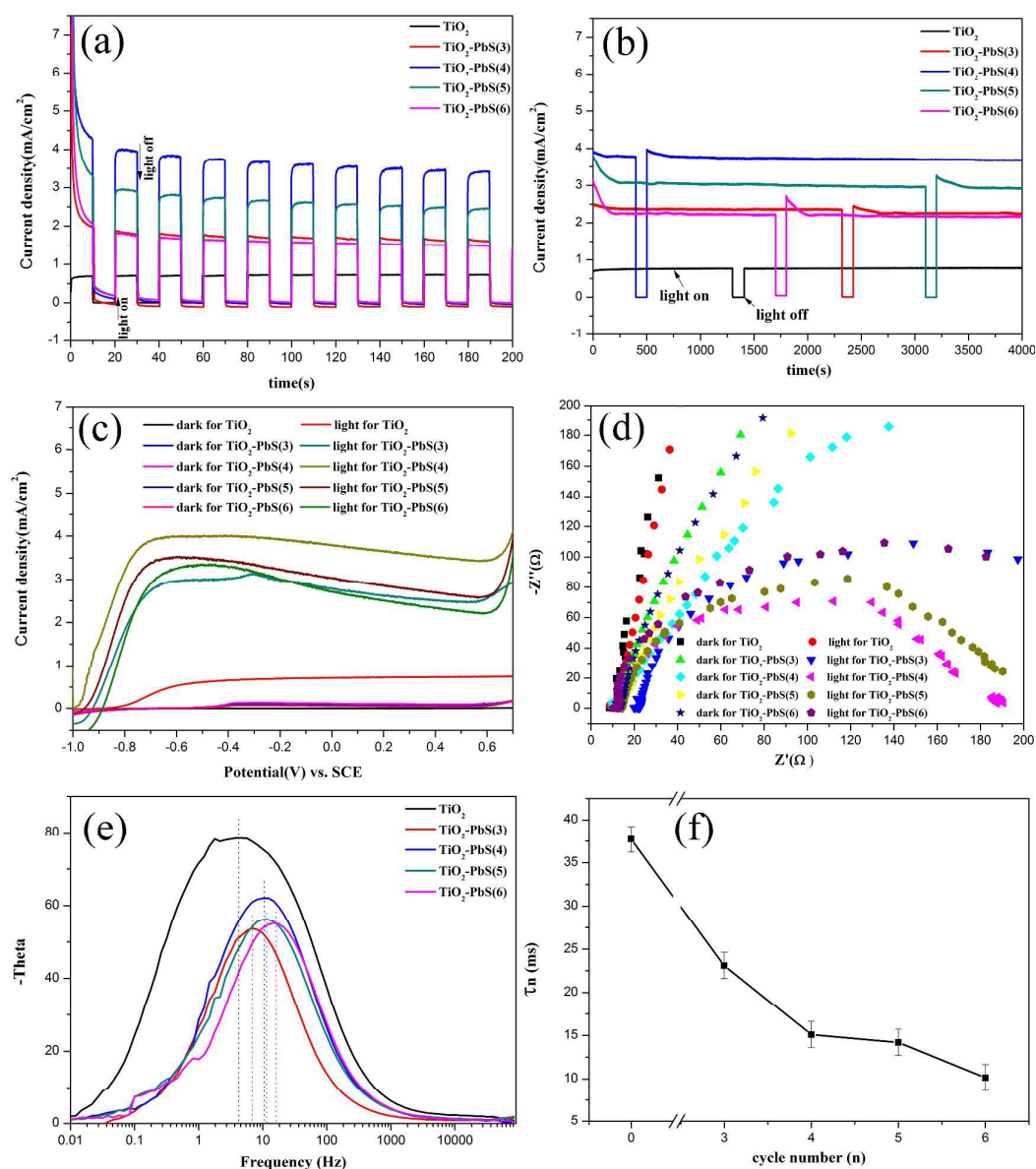
Fig. 5 (a) Transient photocurrent responses and (b) time courses of TiO_2 NRs and $PbS(n)/TiO_2$ photoelectrodes at

the potential of -0.6 V *vs*. SCE under 100 mW cm^{-2} illumination. (c) Linear sweep voltammograms collected under

100 mW cm^{-2} illumination with scan rate of 10 mV s^{-1}. (d) EIS Nynquist plots of TiO_2 NRs and $PbS(n)/TiO_2$

photoelectrodes measured in the dark and under one sun illumination. (e) Bode plots and (f) electron lifetimes of

various photoelectrodes under one sun illumination.

Fig. 5a shows the transient photocurrent responses of the PbS(n)/TiO$_2$ photoelectrodes. When the

samples were illuminated under AM 1.5 at full sun intensity of 100 mW cm^{-2}, all the PbS(n)/TiO$_2$

photoelectrodes exhibited higher photocurrent properties than pure TiO$_2$ NRs. Moreover, the

photocurrent of the PbS/TiO$_2$ photoelectrodes increased along with the SILAR cycle n $\leq$ 4. When n $\geq$ 4,

the photocurrent density decreased, and the photocurrent of PbS(4)/TiO$_2$ photoelectrode was ten times

as high as that of pure TiO$_2$ NRs. Hence, it can be deduced that the amount of PbS QDs deposition on

the TiO$_2$ NRs plays an important role in affecting their photocurrent properties. Although the increasing

quantity of PbS QDs on TiO$_2$ NRs could raise the light absorption, the aggregation of excessive QDs

weakens the quantum size effect and increases the recombination of photo electrons and holes, leading

to the decrease of photocurrent. Fig. 5b shows the time courses for the photocurrent density of various

photoelectrodes. There was no obviously decay of photocurrent under 1 sun illumination, indicating the

high structural and chemical stability of the as-prepared photoelectrodes. In addition, a set of linear

sweep voltammograms were measured in the dark and under 1sun illumination to investigate the PEC

properties, as shown in Fig. 5c. All photoelectrodes show a low dark current with reference to their

respective photocurrent, indicating no fierce electrocatalytic water splitting occurs. Obviously, the

photocurrent of PbS(n)/TiO$_2$ photoelectrodes under illumination increases with the SILAR cycle

number n $\leq$ 4 and decreased when n $\geq$ 4, but still apprently higher than that of bare TiO$_2$ NRs, which is

corresponding to the transient photocurrent responses shown in Fig. 5a and 5b. Furthermore, the onset

potential of photoelectrodes shows a slight shift from -0.886 V$_{SCE}$ for bare TiO$_2$ NRs to -0.986 V$_{SCE}$ for

PbS(4)/TiO$_2$ NRs. The higher photocurrent and lower onset potential indicate more efficient charge

separation and transport in PbS(4)/TiO$_2$ NRs than bare TiO$_2$ NRs[35].

As shown in Fig. 5d, electrochemical impedance measurements (EIS) were conducted on various

photoelectrodes in the dark and under 1 sun illumination with a frequency interval of $10^5 - 10^{-2}$ Hz.

The semicircle corresponds to the electron transfer at the TiO$_2$-QDs/electrolyte interface and transport

in the TiO$_2$. The results suggest that the radius of TiO$_2$ NRs electrodes in dark and one sun illumination

are larger than PbS(n)/TiO$_2$ electrodes due to large band gap of TiO$_2$, which limit the absorption of light

and very small amounts of photo-induced electron can be transferred to FTO film. Moreover, All the

composite electrodes of PbS(n)/TiO$_2$ show smaller resistance-circles under illumination than those in

dark, which can be attributed to the efficient separation of electron-hole pairs and electron injection

between the interfaces of heterojunction and electrolyte for the composite electrodes[29]. The radius of

semicircle decreases with increase of SILAR cycle (n $\leq$ 4), mainly attribute to the increase of the

contact of PbS QDs to electrolyte, which promotes the photo-induced holes collection by S^{2-} in the

electrolyte, facilitates the electron injection from PbS QDs to TiO$_2$ NRs and drains the electrons

transfer in the TiO$_2$ NRs[36]. Fig. 5e shows the bode plots of various photoelectrodes. The plot peak of

the spectrum can be accepted to identify the electron lifetime in these photoelectrodes according to the

following equation[37]:

$$\tau_n = \frac{1}{2\pi f_{min}}$$

The electron lifetime (τ_n) calculated according to Fig. 5e are shown in Fig. 5f. Obviously, the

frequency peak shifts to higher frequencies, corresponding to a decrease of the electron lifetime. It

indicates that τ_n can remain high value, ~37.7 ms, in the TiO$_2$ NRs photoelectrode, which confirm

TiO$_2$ NRs arrays with less crystal defects. The electron lifetime is on the decline with the increase of

PbS QDs. A decrease of the electron lifetime could result from an increase in surface states on the PbS

QDs caused by adhering impurities of the electrolyte. Other possibilities are an increase of

recombination centers inside the electrolyte, or the formation of a new electrolyte compound during the

electrochemical process[37]. However, in our study, the efficiency obtained for the photoelectrode with n

= 4 is higher than that of other photoelectrodes, which can be explained that the optical absorption is

insufficient for photoelectrode with n less than 3, whereas loss of electrons during transport due to

recombination when n higher than 4.
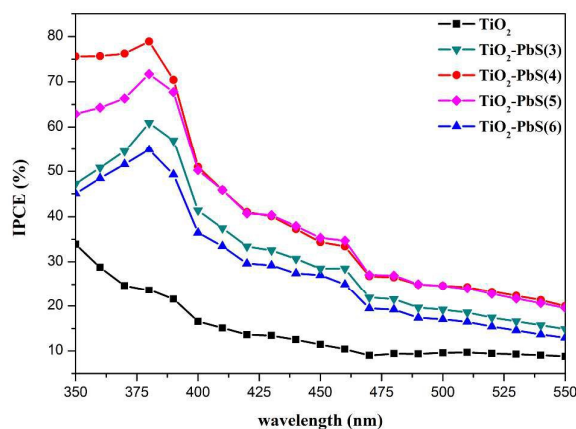
Fig.6 Incident photon to current conversion efficiency (IPCE) spectra of QDSSCs employing

TiO_2/PbS(n) photoelectrodes.

To understand the photogeneration process of the photovoltaic devices, the incident photon to

current conversion efficiency (IPCE) spectra of QDSSCs assembled with TiO_2/PbS(n) photoelectrodes

measured from the I_{sc} monitored at different excitation wavelengths are present in Fig. 6. The value of

IPCE enhances sharply after the SILAR deposition of PbS QDs, indicating the strong injection ability

of photoexcited electrons. The TiO_2/PbS(4) photoelectrode achieves the maximum IPCE of 78.9% in

the wavelength range of 350-450 nm, which suggests that the photovoltaic device with TiO_2/PbS(4)

photoelectrode affords more sufficient light absorption without compromising electron transport and

collection. While raising the SILAR cycle, the photoelectrode suffers from the losses due to the

increased carrier recombination with holes and/or back-electron transfer to the semiconductor QDs.

(a)　　　　　　　　(b)
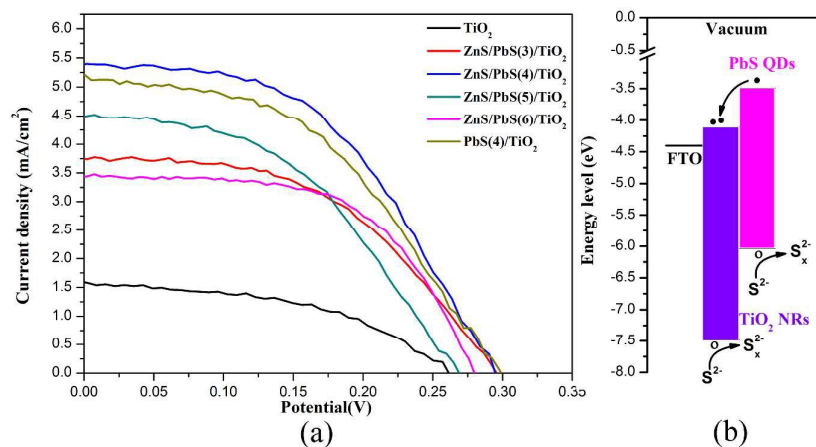
Fig. 7 (a) *J-V* curves of devices employing TiO_2 NRs and PbS(n)/TiO_2 photoelectrodes. (b) Schematic

representation of the energy-level diagram of FTO, TiO_2 NRs , PbS QDs and charge transfer pathways between

PbS and TiO_2 NRs.

Table 2 Parameters obtained from the photocurrent-voltage measurements of the solar cells using

various photoelectrodes.

Sample	J_{sc}(mA cm^{-2})	V_{oc} (mV)	*FF*	*η*
TiO_2	1.59	0.261	0.47	0.20%
ZnS/PbS(3)/TiO_2	3.72	0.295	0.50	0.55%
PbS(4)/TiO_2	5.12	0.299	0.45	0.69%
ZnS/PbS(4)/TiO_2	5.39	0.295	0.48	0.77%
ZnS/PbS(5)/TiO_2	4.50	0.269	0.46	0.57%
ZnS/PbS(6)/TiO_2	3.44	0.280	0.59	0.57%

Fig. 7a shows the characteristics of the experimental photocurrent density-voltage (*J-V*) for the

TiO_2 NRs, PbS(n)/TiO_2 and ZnS/PbS(n)/TiO_2 photoelectrodes with various SILAR cycles under

illumination at one sun light intensity of 100 mW cm^{-2}. As shown in Table 1, the photovoltaic

parameters, including the short-circuit current density (J_{sc}), open-circuit voltage (V_{oc}), fill factor (*FF*)

and power conversion efficiency (*η*) are listed. Apart from the recombination loss of photogenerated

carriers, the recombination of electrons from TiO_2 into the electrolyte also reduces the energy

15

conversion efficiency for QDSSCs. An effective way to retard the back transfer of photoelectrons and protect the QDs from photocorrosion is preparing a ZnS passivation layer according to the literature[38]. Interestingly, we noticed that the introduction of ZnS leads to the increase of η. Consequently, an overall energy conversion efficiency of 0.77% was achieved, resulting a 11.6% increment compared with the value of 0.69% treated without ZnS. The benefit effect of ZnS coating is attributed to the suppression of electron leakage to electrolyte due to efficient passivation of TiO_2 and PbS QDs. In addition, the results demonstrate that the performance of $ZnS/PbS(n)/TiO_2$ devices depends on the value of n. It can be found that the J_{sc} gradually increases from 1.59 to 5.39 mA cm^{-2} when n $\leq$ 4 and the solar cell yields the maximum J_{sc} and a η of 0.77% at the forth cycle. With further increase of SILAR cycles, the J_{sc}, V_{oc} and η values begin to decrease after reaching the maximum value, corresponding to the results observed in Fig. 5(a-c). The thicker semiconductor layers may increase internal recombination of charge carriers in the absorber before the carriers are injected into electron conductors[3], resulting in the decrease of photocurrent density. Furthermore, we can find the V_{oc} exhibits almost the same value at the third and forth cycle, while a tendency of decreasing with the increasing deposition cycles of PbS QDs, which can be ascribe to decrease of the electron lifetime in QDSSCs[39]. This fact is an additional indicator of the presence of internal recombination losses in closely packed QDs.

The energy diagram of the involved components and charge transfer pathways between PbS and TiO_2 NRs are shown in Fig. 7b. When the solar cell is illuminated through the FTO substrate, the PbS QDs and TiO_2 NRs absorb photons and generate electron-hole pairs. The photogenerated excitons divide into electrons and holes on account of the presence of the built-in electric field developed at the interface of PbS QDs and TiO_2 NRs. The photo-induced electrons from PbS can be quickly injected

into TiO$_2$ NRs, arriving at the FTO substrate through the well-aligned crystalline TiO$_2$ NRs. Meanwhile, the photo-induced holes are trapped by S^{2-} in the electrolyte to produce S$_x^{2-}$ [19]. However, the cell performance in this study is still inferior due to the weak driving force of electron injection for PbS QDs although they have the wider absorption compared to other QDs. Thus, further improvement should be made, such as optimizing the quality of PbS QDs and co-sensitizing with other semiconductor QDs. All these investigations are ongoing in our laboratory.

4. Conclusions

In this work, PbS quantum dot-sensitized TiO$_2$ nanorod arrays have been prepared by SILAR method. The details of SILAR cycles for deposition of PbS QDs are discussed and it is found that the performance of PbS QDSSCs depends on the value of n dominantly. The PbS QDs sensitized TiO$_2$ NRs exhibit a signification enhancement in J_{sc} when n = 4, which is attributed to more quantum dots were harvested. Furthermore, the long electron lifetime in the TiO$_2$ make it possible to transfer the photo-induced electrons to FTO substrate. On the other hand, the enlarge absorption edges to the visible region and the effective separation of photogenerated electron-hole pairs at the PbS-TiO$_2$ NRs interface also promote the value of power conversion efficiency. The results confirm that PbS QDs can be used as effective sensitizers for quantum dot-sensitized solar cells.

Acknowledgements

References

1. S. Rühle, M. Shalom and A. Zaban, *ChemPhysChem.*, 2010, **11**, 2290-2304.

2. A. Kongkanand, K. Tvrdy, K. Takechi, M. Kuno and P. V. Kamat, *J. Am. Chem. Soc.*, 2008, **130**,

4007-4015.

3. I. Mora-Seró, S. Giménez, F. Fabregat-Santiago, R. Gómez, Q. Shen, T. Toyoda and J. Bisquert, *Acc. Chem. Res.*, 2009, **42**, 1848-1857.

4. B. A. Gonfa, M. R. Kim, N. Delegan, A. C. Tavares, R. Izquierdo, N. Wu, M. A. El Khakani and D. Ma, *Nanoscale*, 2015, **7**, 10039-10049.

5. S. Mathew, A. Yella, P. Gao, R. Humphry-Baker, F. E. CurchodBasile, N. Ashari-Astani, I. Tavernelli, U. Rothlisberger, K. NazeeruddinMd and M. Grätzel, *Nat. Chem.*, 2014, **6**, 242-247.

6. K. Tvrdy, P. A. Frantsuzov and P. V. Kamat, *Proc. Natl. Acad. Sci.*, 2011, **108**, 29-34.

7. O. E. Semonin, J. M. Luther, S. Choi, H.-Y. Chen, J. Gao, A. J. Nozik and M. C. Beard, *Science*, 2011, **334**, 1530-1533.

8. M. Kapilashrami, Y. Zhang, Y.-S. Liu, A. Hagfeldt and J. Guo, *Chem. Rev.*, 2014, **114**, 9662-9707.

9. K. Lee, A. Mazare and P. Schmuki, *Chem. Rev.*, 2014, **114**, 9385-9454.

10. B. Liu and E. S. Aydil, *J. Am. Chem. Soc.*, 2009, **131**, 3985-3990.

11. C. Han, Z. Chen, N. Zhang, J. C. Colmenares and Y.-J. Xu, *Adv. Funct. Mater.*, 2015, **25**, 221-229.

12. T. Zhang, S. Cui, B. Yu, Z. Liu and D. Wang, *Chem. Commun.*, 2015, **51**, 16940-16943.

13. B. Li, J.-M. Wu, T.-T. Guo, M.-Z. Tang and W. Wen, *Nanoscale*, 2014, **6**, 3046-3050.

14. C. Wang, Z. Chen, H. Jin, C. Cao, J. Li and Z. Mi, *J. Mater. Chem. A*, 2014, **2**, 17820-17827.

15. S. Liu, Z.-R. Tang, Y. Sun, J. C. Colmenares and Y.-J. Xu, *Chem. Soc. Rev.*, 2015, **44**, 5053-5075.

16. B. Weng, S. Liu, Z.-R. Tang and Y.-J. Xu, *RSC Adv.*, 2014, **4**, 12685-12700.

17. J. Tian, R. Gao, Q. Zhang, S. Zhang, Y. Li, J. Lan, X. Qu and G. Cao, *J. Phys. Chem. C*, 2012, **116**, 18655-18662.

18. L. J. Diguna, Q. Shen, J. Kobayashi and T. Toyoda, *Appl. Phys. Lett.*, 2007, **91**, 023116.

19. B. Liu, D. Wang, Y. Zhang, H. Fan, Y. Lin, T. Jiang and T. Xie, *Dalton Trans.*, 2013, **42**, 2232-2237.

20. M. A. Abbas, M. A. Basit, T. J. Park and J. H. Bang, *Phys. Chem. Chem. Phys.*, 2015, **17**, 9752-9760.

21. C. Pilapong, S. Thongtem and T. Thongtem, *J. Nanosci. Nanotechno.*, 2013, **13**, 2189-2192.

22. W. Yue and G. Nie, *J. Nanosci. Nanotechno.*, 2015, **15**, 1312-1319.

23. D. Kumar, G. Agarwal, B. Tripathi, D. Vyas and V. Kulshrestha, *J.Alloy. Compd.*, 2009, **484**, 463-466.

24. Z. Ning, H. Dong, Q. Zhang, O. Voznyy and E. H. Sargent, *ACS Nano*, 2014, **8**, 10321-10327.

25. M. A. Hines and G. D. Scholes, *Adv. Mater.*, 2003, **15**, 1844-1849.

26. H. Lee, M. Wang, P. Chen, D. R. Gamelin, S. M. Zakeeruddin, M. Grätzel and M. K. Nazeeruddin, *Nano Lett.*, 2009, **9**, 4221-4227.

27. E. Rabinovich and G. Hodes, *J. Phys. Chem. C*, 2013, **117**, 1611-1620.

28. S. Arabzade, M. Samadpour and N. Taghavinia, *RSC Adv.*, 2015, **5**, 45592-45598.

29. Y. Wan, M. Han, L. Yu, J. Jia and G. Yi, *RSC Adv.*, 2015, **5**, 78902-78909.

30. M. Han, J. Jia, L. Yu and G. Yi, *RSC Adv.*, 2015, **5**, 51493-51500.

31. J.-R. Huang, X. Tan, T. Yu, L. Zhao and W.-L. Hu, *Electrochim. Acta*, 2014, **146**, 278-287.

32. J. Tang, L. Brzozowski, D. A. R. Barkhouse, X. Wang, R. Debnath, R. Wolowiec, E. Palmiano, L. Levina, A. G. Pattantyus-Abraham, D. Jamakosmanovic and E. H. Sargent, *ACS Nano*, 2010, **4**, 869-878.

33. G. Konstantatos, L. Levina, A. Fischer and E. H. Sargent, *Nano Lett.*, 2008, **8**, 1446-1450.

34. G. Konstantatos and E. H. Sargent, *Appl. Phys. Lett.*, 2007, **91**, 173505.

35. H. Cui, W. Zhao, C. Yang, H. Yin, T. Lin, Y. Shan, Y. Xie, H. Gu and F. Huang, *J. Mater. Chem. A*,

2014, **2**, 8612-8616.

36. T. Hoshikawa, T. Ikebe, R. Kikuchi and K. Eguchi, *Electrochim. Acta*, 2006, **51**, 5286-5294.

37. R. Kern, R. Sastrawan, J. Ferber, R. Stangl and J. Luther, *Electrochim. Acta*, 2002, **47**, 4213-4225.

38. J.-Y. Kim, J. Yang, J. H. Yu, W. Baek, C.-H. Lee, H. J. Son, T. Hyeon and M. J. Ko, *ACS Nano*, 2015, **9**, 11286-11295.

39. D. C. Olson, S. E. Shaheen, M. S. White, W. J. Mitchell, M. F. A. M. van Hest, R. T. Collins and D. S. Ginley, *Adv. Funct. Mater.*, 2007, **17**, 264-269.

Cross-sectional view FESEM images of (a) TiO$_2$ NRs, (b) PbS(4)/TiO$_2$ NRs (The insets show the

top-view of the corresponding Cross-sectional view FESEM images). 3D schematic diagrams of (c)

TiO$_2$ NRs, (d) PbS(4)/TiO$_2$ NRs.